Background-Free Stimulated Raman Spectroscopy and Microscopy

Pascal Berto, Esben Ravn Andresen, and Hervé Rigneault*
Aix-Marseille Université, CNRS, Centrale Marseille, Institut Fresnel, UMR 7249, Domaine Universitaire de Saint Jérôme, F-13397 Marseille Cedex 20, France
(Received 23 September 2013; published 6 February 2014)

We propose a three-color, double-modulation scheme for the background-free detection of stimulated Raman scattering (SRS). We call the scheme stimulated Raman gain and opposite loss detection (SRGOLD). It exploits the symmetric nature of potential parasitic signals (cross phase modulation, two-photon absorption, and thermal effects) to the end of suppressing them. Conversely, the antisymmetric nature of SRS provides for a twofold increase in the magnitude of the SRS signal. We experimentally demonstrate SRGOLD spectroscopy and microscopy on test samples as well as on mice skin samples.

DOI: 10.1103/PhysRevLett.112.053905 PACS numbers: 42.65.Dr, 78.47.nj, 87.57.-s

Although known for more than fifty years, stimulated Raman scattering (SRS) [1,2] was only recently implemented as a contrast mechanism in a microscope yielding label-free chemical imaging with great potential in the biomedical sciences [3–5]. The appeal of SRS is its fast imaging modalities [6], sensitivity orders of magnitude greater than spontaneous Raman scattering, and access to vibrational spectroscopic information that is readily interpretable as Raman spectra [2]. The initial reports suggested that SRS microscopy—unlike its predecessor coherent anti-Stokes Raman scattering (CARS) microscopy [7]—was free of spurious background signal. This is true only in a relative sense; the SRS signal is in general overlaid with parasitic signals stemming from other quasi-instantaneous nonlinear optical processes whose sources are ubiquitous. The ratio of SRS signal to spurious background thus decreases with the concentration and cross section of the Raman scatterers which one seeks to detect. This renders SRS microscopy on biological samples exceedingly difficult in the fingerprint spectral region where molecules present their unique vibrational signature. Indeed, few examples of SRS images in the fingerprint region have been published [8]. The spurious background signals will be spatially nonuniform in heterogenous or scattering samples, which translates into increased risk that parasites will be mistaken for the SRS signal.

The purpose of this Letter is to develop a detection scheme insensitive to parasitic signal that could open the door to reliable SRS imaging in the fingerprint spectral region, in particular, and of weak Raman scatterers, in general. We will first detail the nature of potential sources of parasitic signal, and then we will introduce the principle of the stimulated Raman gain and opposite loss detection (SRGOLD) scheme. We will finally validate the SRGOLD scheme first on model samples, then on a mouse skin sample.

SRS is an energy transfer between a pump pulse and a probe pulse; the pulse at the higher frequency experiences a loss while the one at lower frequency experiences a gain. SRS is particularly appealing because this energy transfer is mediated by optical phonons associated to molecular Raman vibrations whose frequencies equal the frequency difference between the pump and probe beam. SRS stands as a label-free, chemically specific, contrast mechanism as Raman spectra are the fingerprints of molecules. Nonlinear transient absorption and nonlinear transient scattering processes are the two major classes of phenomena that give rise to parasitic signals overlaid on an SRS signal. (i) Nonlinear absorption, also known as two-photon two-color absorption (TPA), arises from the concomitant absorption of one pump and one probe photon. The resulting attenuation of the probe beam is misinterpreted as an SRS signal [9]. (ii) Nonlinear scattering arises from the refractive index change induced by the pump beam and experienced by the probe beam. It is known as cross phase modulation (XPM) when it has a pure nonresonant electronic origin [10] and thermal lensing or thermal scattering [11,12] when it results from temperature-induced refractive index variation. In both cases, nonlinear scattering affects the angular distribution of the probe beam that is further converted into an intensity variation by aperture clipping along the detection beam path. Here again this probe beam intensity variation is misinterpreted as an SRS signal but has no chemical specificity. We report below how an SRS detection scheme can be made free of TPA, XPM, and thermal lensing or scattering artifacts by exploiting the fact that the artifacts are symmetric under sign change of the pump probe frequency difference whereas SRS is antisymmetric. The proposed SRGOLD scheme, furthermore, enhances the chemically specific signal by a factor of 2 and proves to be efficient in heterogeneous samples where linear scattering is at work.

Consider first the standard two-color stimulated Raman gain (SRG) detection scheme often employed in SRS microscopy. The involved pump and probe frequencies are $\omega_0 + \Omega$ and ω_0, with Ω the targeted vibrational molecular frequency. Figure 1(a) details the energy transfer

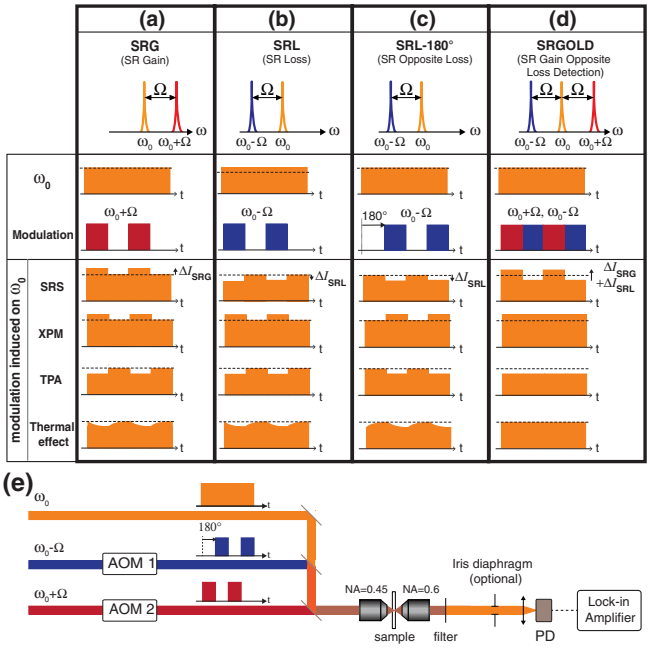

FIG. 1 (color online). SRGOLD principle and practical implementation. [(a)–(d)] Sketch of incident pumps ($\omega_0 + \Omega$, red, or $\omega_0 - \Omega$, blue) and probe (ω_0, orange) and modulation transfer to the probe in (a) SRG scheme, (b) SRL scheme, (c) stimulated Raman opposite loss (SRL-180°) scheme, and (d) SRGOLD scheme. Comparison of (a) to (c): The modulations induced on the probe due to SRS are in phase while the artifacts induced by XPM, TPA, and the thermal effect are in opposite phase. Conclusion on (d): In the SRGOLD scheme, the SRG and SRL signals add up while the artifacts cancel out. (e) Practical SRGOLD implementation.

to ω_0 from the intensity-modulated $\omega_0 + \Omega$ due to SRS as well as the three effects responsible for artifacts: XPM, TPA, and thermal effects. While SRS results in a gain ΔI_{SRG} at ω_0, the Kerr lens resulting from XPM changes the divergence of ω_0 that due to aperture clipping is interpreted as a gain or a loss. Likewise, the effect of the thermal lens is interpreted as a gain or a loss. In Fig. 1, we arbitrarily assume a gain for XPM and a loss for thermal effects. TPA always results in attenuation at ω_0 and is always interpreted as a loss.

Consider now the standard two-color stimulated Raman loss (SRL) scheme also employed in SRS microscopy where the involved pump and probe frequencies are $\omega_0 - \Omega$ and ω_0. Note that the difference compared to the SRG scheme is a sign change on the frequency difference Ω. Figure 1(b) details the energy transfer to ω_0 from the intensity-modulated $\omega_0 - \Omega$. The antisymmetry of SRS is readily appreciated by comparison with what is seen in Fig. 1(a); SRS now results in a loss ΔI_{SRL} rather than a gain. Conversely, the XPM, TPA, and thermal artifacts are seen to be symmetric; they are unchanged compared to that in Fig. 1(a).

Figure 1(c) again shows a standard two-color SRL process but for $\omega_0 - \Omega$ modulation phase shifted by 180° (denoted SRL-180°) as compared to that of Fig. 1(b). Consequently, SRL signal and the XPM, TPA, and thermal artifacts are similarly phase shifted.

The SRGOLD scheme in Fig. 1(d) comes about as the addition of SRG seen in Fig. 1(a) and SRL-180° seen in Fig. 1(c). Here, the three frequencies $\omega_0 - \Omega$, ω_0, and $\omega_0 + \Omega$ are incident on the sample whereas $\omega_0 - \Omega$ and $\omega_0 + \Omega$ are modulated in opposite phase. The net effect is (1) to multiply by 2 the SRS signal at ω_0 as it experiences successively a loss and a gain ($\Delta I_{\mathrm{SRG}} + \Delta I_{\mathrm{SRL}}$) and (2) to cancel all the parasitic effects, namely, XPM, TPA, and thermal effects. The physical picture of the cancellation is that the XPM, TPA, and thermal effects are made perpetual in the SRGOLD scheme to which signal detection by modulation transfer is insensitive.

In practice, the implementation of SRGOLD proceeds as presented in Fig. 1(e). The three IR beams are provided by a commercially available synchronously pumped OPO system (APE Levante OPO pumped by a frequency doubled Nd:YVO, picotrain HighQ laser) $\omega_0 - \Omega = 1150$–2450 nm (tunable idler beam), $\omega_0 = 1064$ nm, and $\omega_0 + \Omega = 690$–990 nm (tunable signal beam). These three beams (pulse duration ~5 ps, repetition rate 76 MHz) are overlapped in time and space and sent into a custom-made scanning microscope [13]. The signal at ω_0 is detected in the forward direction by means of a high-speed photodiode (Thorlabs PDA10CS) and a fast lock-in amplifier (Signal Recovery 7280). Idler ($\omega_0 - \Omega$) and signal ($\omega_0 + \Omega$) beams are modulated at 1.5 MHz in opposite phase by two acousto-optic modulators (AAOptoelectronic MT200 A0,2-800). The collection objective lens (NA = 0.6, LUCPlanFL N 20×, Olympus) has a larger numerical aperture than the excitation one (NA = 0.45, LCLPLN 20× IR, Olympus) to minimize the parasitic nonlinear scattering (XPM, thermal lensing or scattering) effects. For imaging, the sample is raster scanned.

As a first experimental demonstration, we performed SRGOLD spectroscopy. Figure 2(a) presents the stimulated Raman spectra of pure chlorobenzene as recorded in SRG, SRL, SRL-180°, and SRGOLD schemes. These spectra were recorded with an iris diaphragm located before the photodiode [see Fig. 1(e)] in order to exemplify the contribution of XPM. Indeed, TPA and thermal lensing have negligible contribution in chlorobenzene at the considered IR wavelengths due to its transparency. In Fig. 2(a), SRG and SRL-180° spectra have different negative and positive offsets. These result from the XPM Kerr lens experienced by ω_0 while interacting with $\omega_0 + \Omega$ and $\omega_0 - \Omega$ (180° phase shifted). In this case, the refractive index variations in the SRG and SRL cases experienced by the ω_0 are given by

$$\delta n_{\omega_0}^{\omega_0+\Omega} = 3\frac{\chi^{(3)}_{\mathrm{XNR}}(\omega_0+\Omega)I_{\omega_0+\Omega}}{n(\omega_0)n(\omega_0+\Omega)\epsilon_0 c}$$
$$\delta n_{\omega_0}^{\omega_0-\Omega} = 3\frac{\chi^{(3)}_{\mathrm{XNR}}(\omega_0-\Omega)I_{\omega_0-\Omega}}{n(\omega_0)n(\omega_0-\Omega)\epsilon_0 c} \quad (1)$$

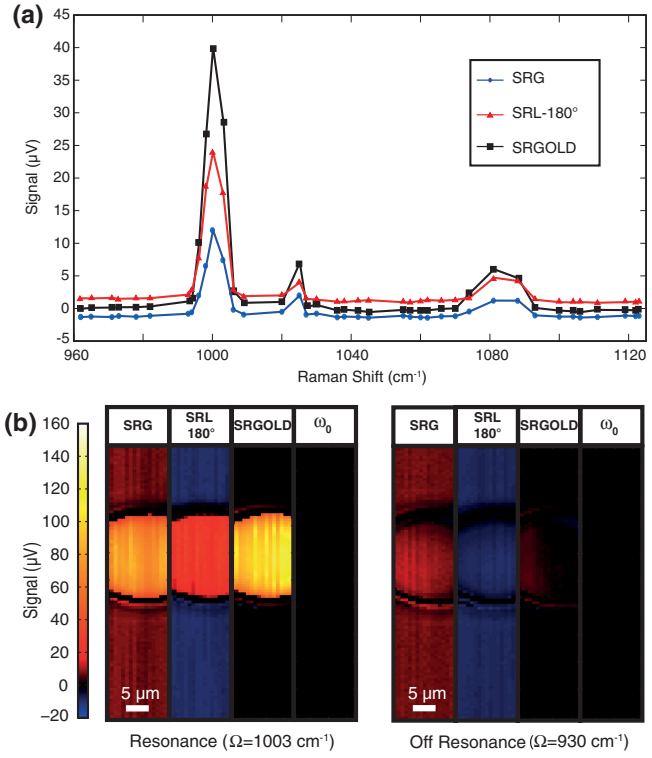

FIG. 2 (color online). SRGOLD spectroscopy and microscopy. (a) Stimulated Raman spectra of chlorobenzene as recorded in stimulated Raman gain (SRG, blue circles), stimulated Raman loss (SRL-180°, red triangles), and SRGOLD (black squares) schemes. The spectral offsets seen in SRG and SRL-180° are canceled in SRGOLD over the 160 cm^{-1} recorded band. (b) 20 μm polystyrene bead imaging with the SRG, SRL-180°, and SRGOLD schemes. At C–C molecular resonance ($\Omega = 1003$ cm^{-1}) and off resonance ($\Omega = 930$ cm^{-1}); the background offsets seen in SRG and SRL-180° are absent from the SRGOLD images while the signal is the sum of the SRG and SRL-180° ones. The ω_0 image is the unmodulated ω_0 signal, with the sample present and with $\omega_0 + \Omega$ and $\omega_0 - \Omega$ blocked. Image 101×17 pixels, $I_{\omega_0+\Omega} = 70$ mW, $I_{\omega_0} = 160$ mW, $I_{\omega_0-\Omega} = 30$ mW, pixel dwell time 5 ms.

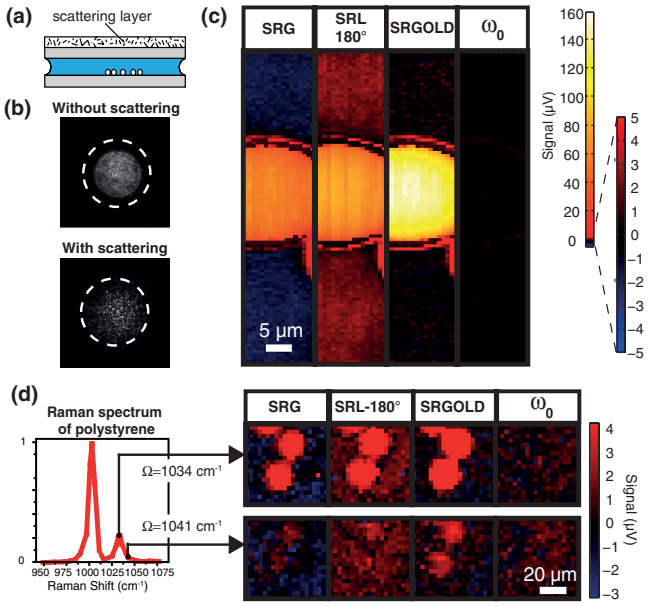

FIG. 3 (color online). SRGOLD in scattering test samples. (a) Model sample with a scattering top layer. (b) Image of the back aperture of the collection objective showing how ω_0 is clipped in the presence of scattering. (c) SRG, SRL-180°, and SRGOLD images of 20 μm polystyrene beads in the presence of scattering layer; the color scale is the same as that in Fig. 2(b). Image 101×17 pixels, $I_{\omega_0+\Omega} = 60$ mW, $I_{\omega_0} = 50$ mW, $I_{\omega_0-\Omega} = 50$ mW, pixel dwell time 10 ms. (d) SRG, SRL-180°, and SRGOLD images of polystyrene beads for weak Raman bands at $\Omega = 1034$ and 1041 cm^{-1}.

where $I_{\omega_0+\Omega}$ and $I_{\omega_0-\Omega}$ are the signal and idler intensity, respectively, ϵ_0 is the vacuum permittivity, and c is the speed of light. In Eq. (1), $\chi^{(3)}_{\mathrm{XNR}}$ are the cross phase nonlinear susceptibilities given by $\chi^{(3)}_{\mathrm{XNR}}(\omega_0 + \Omega) = \chi^{(3)}(-\omega_0, \omega_0 + \Omega, \omega_0, -(\omega_0 + \Omega))$ and $\chi^{(3)}_{\mathrm{XNR}}(\omega_0 - \Omega) = \chi^{(3)}(-\omega_0, \omega_0 - \Omega, \omega_0, -(\omega_0 - \Omega))$ that are assumed to be independent of frequency. It is possible to set $\delta n^{\omega_0+\Omega}_{\omega_0} = \delta n^{\omega_0-\Omega}_{\omega_0}$ by adjusting the ratio $(I_{\omega_0+\Omega})/(I_{\omega_0-\Omega})$ while being off molecular resonance. In this case, the XPM Kerr lens effects experienced by ω_0 while interacting sequentially with $\omega_0 + \Omega$ and $\omega_0 - \Omega$ are set equal and the resulting net effect is the cancellation of the XPM background. In Fig. 2(a) this XPM cancellation was performed at $\Omega = 960$ cm^{-1}. This cancellation is also accompanied by a significant signal improvement.

Figure 2(b) shows an example of SRGOLD microscopy. A 20 μm polystyrene bead, embedded in a nonresonant liquid (Cargille immersion liquid OHZB), is successively imaged in the SRG, SRL-180°, and SRGOLD modalities both on the C–C skeletal vibrational resonance ($\Omega = 1003$ cm^{-1}) and off resonance ($\Omega = 930$ cm^{-1}). Here again, an iris diaphragm is placed before the photodiode to exemplify the effect of XPM. Whereas SRG and SRL images present a significant XPM background both at and off resonance, the SRGOLD scheme is completely background free and shows a signal at resonance that is the summation of the SRG and SRL-180° signals. The "ω_0" image is the signal with the sample present and with $\omega_0 + \Omega$ and $\omega_0 - \Omega$ beams blocked. This image represents the instrumental background in the detection scheme; i.e., SRGOLD is deemed successful if it can decrease the image background to this level.

We wish now to evaluate the SRGOLD modality in a more realistic case when the sample presents scattering, a situation that is found when imaging biological tissues. We concentrate first on a model sample consisting of 20 μm polystyrene beads sandwiched between two cover slips (spacing 150 μm) on the top of which a 60 μm scattering layer (Scotch tape 3 M) is placed [Fig. 3(a)]. The iris diaphragm [Fig. 1(e)] is now removed. Figure 3(b) shows

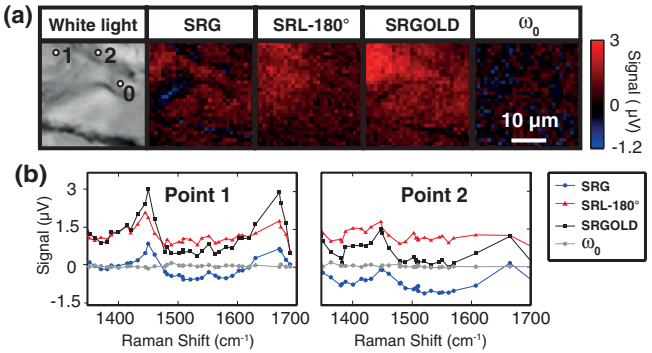

FIG. 4 (color online). SRGOLD in biological samples. (a) white light, SRG, SRL-180°, and SRGOLD images of a 20 μm thick mouse skin sample for the amide II ($\Omega = 1450$ cm^{-1}) resonance. SRGOLD artifact balance is performed at point 0. The ω_0 image is the ω_0 signal with the sample present and with $\omega_0 + \Omega$ and $\omega_0 - \Omega$ beams blocked. Image 30×30 pixels, $I_{\omega_0+\Omega} = 86$ mW, $I_{\omega_0} = 33$ mW, $I_{\omega_0-\Omega} = 40$ mW, pixel dwell time 50 ms. (b) SRG (blue circles), SRL-180° (red triangles), and SRGOLD (black squares) spectra as recorded in points 1 and 2. Superimposed is the ω_0 signal only (gray circles). SRGOLD proves to cancel artifact over the 1350 cm$^{-1} < \Omega < 700$ cm^{-1} band.

images of the ω_0 laser light at the collection objective lens back aperture when the scattering layer is present and not present. In the absence of scattering layer, the collection objective lens (NA = 0.6) collects the totality of the focused (NA = 0.45) ω_0 beam, whereas this is not the case when the scattering layer is present since this results in overfilling the collection lens back aperture. In this situation, the collection objective is clipping the ω_0 beam and XPM background is expected. Figure 3(c) shows the SRG, SRL-180°, and SRGOLD images of a polystyrene bead at resonance ($\Omega = 1003$ cm^{-1}) in the presence of the scattering layer. In this example, SRGOLD is efficient at removing the XPM background that is clearly present on the SRG and SRL images while it also proves to be efficient in enhancing image contrast in the presence of scattering for weak Raman bands. Figure 3(d) shows the SRG, SRL-180°, and SRGOLD images of polystyrene beads at $\Omega = 1034$ and 1041 cm^{-1} in the presence of the scattering layer. These two vibrational bands are 10 and 50 times weaker than the previously considered $\Omega = 1003$ cm^{-1} C–C band, respectively. In both cases, the SRGOLD image is of superior quality and makes the beads stand out more clearly for the $\Omega = 1041$ cm^{-1} case.

In order to evaluate the ability of SRGOLD to reveal vibrational contrast in biological samples, we concentrate now on its implementation in mice skin samples. Samples of 20 μm thick cryosectioned mice skin were placed on cover slips for SRS investigation without any further preparation. Figure 4(a) shows a white light image of a selected skin sample together with the SRG, SRL-180°, and SRGOLD images when targeting the amide II band at $\Omega = 1450$ cm^{-1}. Note that this amide band is about 10 times weaker than the $\Omega = 2950$ cm^{-1} CH_3 stretch commonly imaged with CARS and SRS. The ω_0 image presents, as before, the SRGOLD image with $\omega_0 + \Omega$ and $\omega_0 - \Omega$ beams blocked. In the SRGOLD scheme, the artifact balance [realized by adjusting $(I_{\omega_0+\Omega})/(I_{\omega_0-\Omega})$] was performed arbitrarily at point 0 for off resonance frequency $\Omega = 1550$ cm^{-1}. Whereas SRG and SRL images show a poor contrast, the SRGOLD image correlates much better with the white light image showing details invisible with conventional SRG and SRL contrast mechanisms. To further appreciate the spectroscopic ability of the SRGOLD scheme, Fig. 4(b) presents the SRG (blue circles), SRL-180° (red triangles), and SRGOLD (black squares) spectra in the amide band (1350cm$^{-1} < \Omega < 1700$ cm^{-1}) obtained by scanning $\omega_0 + \Omega$ and $\omega_0 - \Omega$ [13]. On the same graph is also shown the signal with $\omega_0 + \Omega$ and $\omega_0 - \Omega$ blocked (gray circles). Two sets of spectra are presented here at points 1 and 2 as labeled in the white light image in Fig. 4(a). The opposite signs of the backgrounds in the SRG and SRL spectra prove that artifacts (XPM, TPA, thermal) are at work. Those are significantly suppressed in the SRGOLD spectra at both points 1 and 2. We can appreciate that the SRGOLD artifact balance performed at point 0 holds over most of the field of view and can be practically used over an area as large as 200×200 μm depending on the sample. Although SRGOLD artifact can be nicely balanced spatially over a quite large field of view, the balance as a function of frequency deserves some more attention. Indeed, contrary to XPM, TPA can exhibit chromatism between $(\omega_0) + (\omega_0 + \Omega) = 2\omega_0 + \Omega$ and $(\omega_0) + (\omega_0 - \Omega) = 2\omega_0 - \Omega$. For $2\omega_0 + \Omega$ the magnitude and slope of the absorption of endogenous proteins is larger than that for $2\omega_0 - \Omega$. Therefore, the TPA artifact changes faster with frequency in the SRG scheme than it does in the SRL scheme. We have found that, in the 1000 cm$^{-1} < \Omega <$ 1700 cm^{-1} range, the artifact cancellation in SRGOLD holds over 400 cm^{-1} without further adjusting $(I_{\omega_0+\Omega})/(I_{\omega_0-\Omega})$ (see the Supplemental Material Fig. S1 [14]).

The proposed SRGOLD scheme uses the fundamental antisymmetric nature of SRS and the symmetric nature of potential artifacts (XPM, TPA, and thermal effects) to cancel all spurious signals not pertaining to Raman processes. Not only does it provide true background-free SRS imaging and spectroscopy, it also enhances by a factor of 2 the SRS signal. This is because in SRGOLD, one is not modulating between on and off resonance. Rather, one is modulating between SRG detection and SRL detection. No post processing nor *a priori* knowledge of the targeted Raman band is required. The experimental implementation of SRGOLD is straightforward and takes full advantage of the commercial OPO source technology that generates at the same time $\omega_0 - \Omega$, ω_0, and $\omega_0 + \Omega$ over the full molecular vibrational spectrum. All these features are unique to the SRGOLD scheme and differ fundamentally from previously reported efforts aimed at improving the

sensitivity in SRS [15–17]. Whereas the artifact cancellation has been demonstrated here in the forward detection scheme, it would also work in the backward detection modality as the XPM, TPA, and thermal effects are made perpetual and, hence, invisible to the lock-in detection. We believe SRGOLD can bring valuable sensitivity and signal to noise ratio enhancement in label-free molecular imaging and spectroscopy.

The authors acknowledge financial support from the Centre National de la Recherche Scientifique (CNRS), the EU COST MicroCoR network, the Weizmann NaBi European Associated Laboratory, ANR Grant France Bio Imaging (No. ANR-10-INSB-04-01) and France Life Imaging (No. ANR-11-INSB-0006) infrastructure networks, and the "Region Provence Alpes Cote d'Azur."

*Corresponding author.
herve.rigneault@fresnel.fr

[1] E. J. Woodbury and W. K. Ng, Proc. IRE **50**, 2367 (1962).
[2] N. Bloembergen, Am. J. Phys. **35**, 989 (1967).
[3] C. W. Freudiger, W. Min, B. G. Saar, S. Lu, G. R. Holtom, C. He, J. C. Tsai, J. X. Kang, and X. S. Xie, Science **322**, 1857 (2008).
[4] P. Nandakumar, A. Kovalev, and A. Volkmer, New J. Phys. **11**, 033026 (2009).
[5] Y. Ozeki, F. Dake, S. Kajiyama, K. Fukui, and K. Itoh, Opt. Express **17**, 3651 (2009).
[6] B. G. Saar, C. W. Freudiger, J. Reichman, C. M. Stanley, G. R. Holtom, and X. S. Xie, Science **330**, 1368 (2010).
[7] E. J. Sanchez, L. Novotny, and X. S. Xie, Phys. Rev. Lett. **82**, 4014 (1999).
[8] Y. Ozeki, W. Umemura, Y. Otsuka, S. Satoh, H. Hashimoto, K. Sumimura, N. Nishizawa, K. Fukui, and K. Itoh, Nat. Photonics **6**, 845 (2012).
[9] D. Fu, T. Ye, G. Yurtsever, W. S. Warren, and T. E. Matthews, J Biomed. Opt. **12**, 054004 (2007).
[10] P. Samineni, B. Li, J. W. Wilson, W. S. Warren, and M. C. Fischer, Opt. Lett. **37**, 800 (2012).
[11] S. Berciaud, D. Lasne, G. A. Blab, L. Cognet, and B. Lounis, Phys. Rev. B **73**, 045424 (2006).
[12] S. Lu, W. Min, S. Chong, G. R. Holtom, and X. S. Xie, Appl. Phys. Lett. **96**, 113701 (2010).
[13] S. Brustlein, P. Ferrand, N. Walther, S. Brasselet, C. Billaudeau, D. Marguet, and H. Rigneault, J Biomed. Opt. **16**, 021106 (2011).
[14] See Supplemental Material at http://link.aps.org/supplemental/10.1103/PhysRevLett.112.053905 for spectral dependence of two-photon absorption (TPA) artefact.
[15] G. C. Bjorklund, Opt. Lett. **5**, 15 (1980).
[16] K. I. Popov, A. F. Pegoraro, A. Stolow, and L. Ramunno, Opt. Lett. **37**, 473 (2012).
[17] D. Zhang, M. N. Slipchenko, D. E. Leaird, A. M. Weiner, and J. X. Cheng, Opt. Express **21**, 13864 (2013).